Structural Durability & Health Monitoring

Tech Science Press

https://doi.org/10.32604/sdhm.2026.081014

ARTICLE

Effects of Recycled Brick Powder on Thermal, Mechanical Properties, and Pore Structure of Alkali-Activated Foam Concrete

Xinzhan Li[1], **Haixin Sun**[2], **Li Li**[1,3,*], **Zongjin Li**[3], **Guangming Xie**[4] and **Guangzhao Li**[4]

[1]College of Water Resources and Architectural Engineering, Northwest A & F University, Yangling, China
[2]Sichuan Water Development Investigation Design & Research Co., Ltd., Chengdu, China
[3]Faculty of Innovation Engineering, Macau University of Science and Technology, Avenida Wai Long, Taipa, Macao SAR, China
[4]Kailuan Energy Chemical Co., Ltd., Tangshan, China

*Corresponding Author: Li Li. Email: drlili@nwafu.edu.cn

Received: 21 February 2026; Accepted: 30 April 2026; Published: 24 August 2026

ABSTRACT: To utilize waste clay bricks and reduce carbon emissions, recycled brick powder (RBP) was prepared from waste brick-concrete structures and used to produce alkali-activated slag-recycled brick powder foam concrete (ASRFC). This paper evaluated the impact of RBP replacement rates and water-binder ratio on the physical and mechanical properties of foam concrete, including its thermal conductivity, strength, and pore structure. The results demonstrated that the addition of 10% RBP resulted in decreases in the apparent density and thermal conductivity of ASRFC, while flexural strength and the flexural-compressive strength ratio exhibited significant increases. These phenomena can all be attributed to a reduction in the fractal dimension of the pores and a more uniform pore size distribution. However, when the RBP replacement rate exceeded 20%, the enhancement of pore structure was diminished, the strength of ASRFC was reduced, while the water absorption rate and thermal conductivity exhibited a significant increase. As the water-to-binder ratio (W/B) increases, the compressive strength of ASRFC displays a slight improvement, while the flexural strength and flexural-to-compressive strength ratio exhibit a significant decrease. The parameters of pore fractal dimension, pore size distribution, and thermal conductivity demonstrate a tendency to initially decrease and subsequently increase, with the optimal W/B determined to be 0.45. A significant correlation has been identified between the pore fractal dimension and thermal conductivity/strength of alkali-activated foam concrete.

KEYWORDS: Alkali-activated materials; recycled brick powder; foam concrete; physical and mechanical properties; pore structure

1 Introduction

Foam concrete is a type of lightweight, porous material that is utilized extensively in the construction, transportation [1], and energy sectors due to its low density, excellent thermal insulation and fire resistance properties, sound absorption capabilities [2,3], and other superior characteristics [4,5]. The material demonstrates remarkable insulation performance and noise reduction capabilities, making it particularly valuable for diverse urban applications [6,7]. Nevertheless, the elevated cement utilization in the production of foam concrete frequently engenders substantial carbon dioxide emissions. Consequently, the development of green, low-carbon, high-performance porous lightweight materials is of significant importance for their widespread application in prefabricated buildings, energy-saving insulation components, and backfill projects [5,8].

Copyright © 2026 The Authors. Published by Tech Science Press. This work is licensed under a Creative Commons Attribution 4.0 International License, which permits unrestricted use, distribution, and reproduction in any medium, provided the original work is properly cited.

Moreover, with the acceleration of global urbanization, there has been a dramatic surge in the stock and growth of construction waste in various countries, with global annual C&D waste exceeding 1 billion tonnes [9]. According to the statistics provided by Wang et al. [10], in 2018, waste bricks and waste concrete accounted for over 80% of China's total construction and demolition waste, with a utilization rate of less than 30%. In recent years, slag-based polymer foam concrete has emerged as a research focus in the field of green building materials [11]. This is due to its low carbon emissions, high-temperature resistance, and low thermal conductivity, among other advantageous physical and mechanical properties [12,13]. The high reactivity of slag during the early stages of hydration is the foundation for the excellent physical and mechanical properties of concrete. In this study, RBP, which has been prepared by grinding waste clay bricks, has been found to contain a high content of SiO_2 and Al_2O_3, in addition to a porous structure. A large body of research indicates that different pore structure parameters have a significant impact on macroscopic properties, with the fractal dimension of the pores having a particularly pronounced effect on mechanical properties and thermal insulation behaviour [14,15]. However, the literature on the use of brick powder for the preparation of alkali-activated foamed concrete remains limited. The neglect of the coupling effect between the water-to-binder ratio (W/B) and RBP, as well as the lack of quantitative studies on the correlation between pore structure and macroscopic properties, has hindered the application of alkali-activated brick powder foamed concrete in building envelope materials and other fields.

To bridge the existing research gap, this study fabricated lightweight and high-strength ASRFC using slag and waste brick powder as raw materials and fillers. The effects of water-to-binder ratio and brick powder content on the thermal, mechanical, and pore structural properties of ASRFC were systematically investigated. Specifically, this research highlights the influence of pore structural characteristics (fractal dimension and pore size distribution) on various macroscopic properties, and effectively establishes the relationship between the macro-mechanical properties and meso-scale pore structure of alkali-activated slag-brick powder foam concrete. These findings provide experimental data and theoretical guidance for their application in building thermal insulation materials, while promoting the high-value utilization of waste clay bricks.

2 Materials and Experiments

2.1 Materials

The primary cementitious materials utilized in this study were S95 slag (Henan Binrong Casting Materials Co., Ltd.) and brick powder (obtained by crushing and screening construction waste from demolished brick-concrete structures). The brick powder particles were subjected to a screening process through a 1.18 mm sieve, after which they were subjected to a 10-min planetary ball milling process (with five minutes of forward and reverse rotation at a speed of 350 rpm, and a feed ratio of two-thirds of the ball mill tank capacity). The ball mill was manufactured by Changsha Taizhong Powder Technology Co., Ltd. and is equipped with four 500 mL ball milling jars. The grinding balls in the ball milling jars consist of four different diameters of stainless steel balls, namely 4, 6, 8, 12, and 14 mm, with proportions of 24%, 26%, 28%, 12%, and 10%, respectively. The chemical composition, content, and particle size distribution of the slag and brick powder used in this study are shown in Fig. 1 and Table 1. The specific surface areas of the slag and brick powder are 1300 and 577 m^2/g, respectively. The alkaline activator employed in this study was a sodium silicate solution, manufactured by Henan Gongyi Changlong Sodium Silicate Factory. The sodium silicate solution exhibited a sodium oxide (Na_2O) content of 9.0%, accompanied by a silicon dioxide (SiO_2) content of 28.08%. This is indicative of a modulus of 3.224. In this experiment, solid sodium hydroxide (AR, Guangdong Guanghua Technology Co., Ltd.) was utilized to reduce the water glass modulus to 1.5.

Hydrogen peroxide and calcium stearate were utilized as foaming agents and foam stabilizers, respectively. All experiments were conducted using tap water (temperature: 20 ± 2°C).

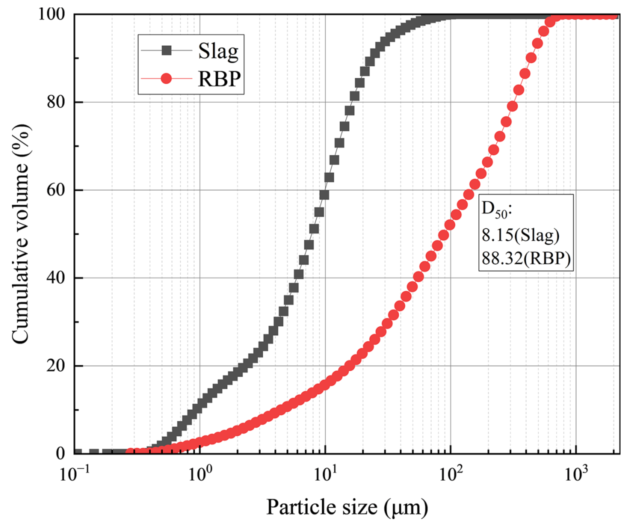

Figure 1: The particle size distribution of Slag and RBP.

Table 1: Chemical composition of RBP and Slag (%).

Component	CaO	SiO_2	Al_2O_3	MgO	SO_3	Fe_2O_3	K_2O	MnO
Slag	35.40	35.07	14.91	7.51	2.34	0.92	0.49	0.36
RBP	54.00	13.96	17.34	2.28	0.88	–	2.71	–

2.2 Preparation of Foam Concrete

The preparation process of this experiment is illustrated in Fig. 2. The preparation of ASRFC comprises two distinct stages: the initial mixing stage and the subsequent foaming mixing stage. In the subsequent stage of the process, namely the mixing stage, the following ingredients are dry-mixed at a low speed for a period of five minutes: slag, brick powder, and calcium stearate. Subsequently, water glass and additional water are added and mixed for 2 min. In the foaming mixing stage, H_2O_2 is added, and the mixture is thoroughly foamed through high-speed stirring. Samples measuring 40 mm × 40 mm × 160 mm, 100 mm × 100 mm × 100 mm, and 300 mm × 300 mm × 30 mm were molded to assess the physical and mechanical properties of the foam concrete. After demoulding for 24 h, the samples were immersed in a constant-temperature water bath at (20 ± 2)°C for curing. Table 2 presents the blend proportions of the slurry. In this study, the water-to-binder ratio (W/B) is defined as the mass ratio of water to the total cementitious materials, where the cementitious materials consist of slag and RBP.

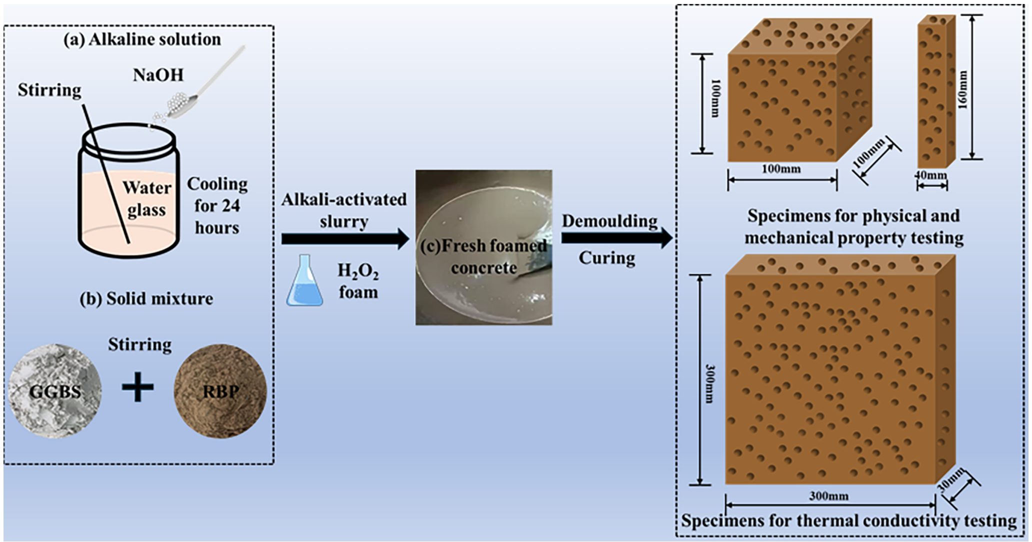

Figure 2: Process flow chart of preparation.

Table 2: Mix proportions of geopolymer foam concrete (g).

No.	Slag	RBP	Water Glass	Water	H_2O_2	Calcium Stearate
W35B0	1000	0		174.15		
W35B1	900	100		174.15		
W35B2	800	200		174.15		
W35B3	700	300		174.15		
W40B0	1000	0		224.15		
W40B1	900	100		224.15		
W40B2	800	200		224.15		
W40B3	700	300	478.25	224.15	40	10
W45B0	1000	0		274.15		
W45B1	900	100		274.15		
W45B2	800	200		274.15		
W45B3	700	300		274.15		
W50B0	1000	0		324.15		
W50B1	900	100		324.15		
W50B2	800	200		324.15		
W50B3	700	300		324.15		

Note: The quantities of water glass, H_2O_2, and calcium stearate remain constant across all groups.

2.3 Characterization and Test Methods

2.3.1 Spread Test

The spread of geopolymer foam concrete was measured in accordance with the standard GB/T8077-2000 "*Test Methods for Homogeneity of Concrete Admixtures*".

2.3.2 Mechanical Properties Test

Following the Chinese standard JG/T 266–2011 *"Foam Concrete,"* the dry density and water absorption of the samples were measured. The compressive and flexural properties of ASRFC at 1, 3, 7, 14, and 28 d were tested by using a 10 kN universal testing machine.

2.3.3 Thermal Conductivity Test

Following the "Protection Hot Plate Method for Determining Steady-State Thermal Resistance and Related Properties of Thermal Insulation Materials" (GB/T10294), the thermal conductivity of 300 mm × 300 mm × 30 mm specimens was measured.

2.3.4 Pore Structure Measurement

The analysis of the pore structure characteristics was conducted through the utilization of the image method in the present study. Initially, the surface area of the dried cubic specimen (100 mm × 100 mm) was obtained through slicing, and subsequently, the surface was photographed using an optical microscope and a mobile phone. As demonstrated in Fig. 3, the microscopic image of the foam concrete contour was initially binarized, and subsequently, the fractal dimension (FD) was derived using the box counting (BC) process [16]. Concurrently, the binarized images were utilized for the measurement and statistical analysis of pore size, thereby facilitating the determination of the pore size distribution.

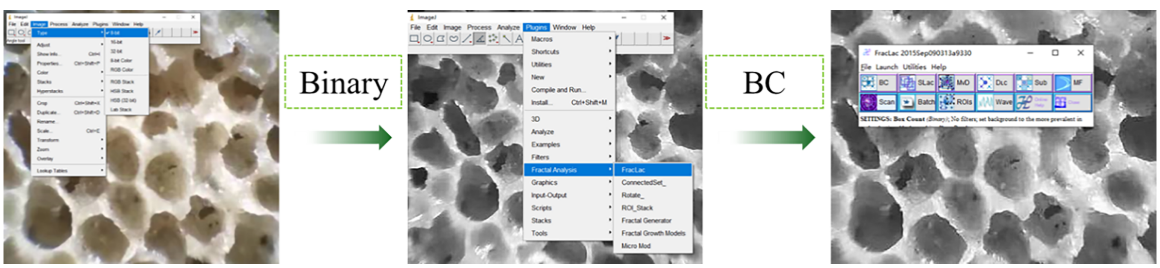

Figure 3: Calculation method of FD.

2.3.5 Microstructural Analysis

To thoroughly analyze the composition of hydration products and the characteristics of pore morphology in FC, this study employed XRD and SEM for phase and microstructure characterization of the specimens. XRD Analysis: specimens cured to the specified age were ground into fine powder and analyzed for phase composition using an X-ray diffractometer. The test conditions included a scanning range of 5° to 90° and a step scanning rate of 10°/min. The obtained diffraction patterns were processed using MDI Jade software and analyzed by phase to determine the types of main hydration products. SEM and EDS observation: The specimens that had undergone standard curing were selected and cut into small chunks of roughly 1 cm^3, and then immediately immersed in absolute ethanol to halt the hydration reaction. The specimens were subsequently dehydrated and polished to obtain a smooth surface. A thin layer of gold was coated onto the surface to improve electrical conductivity. The microscopic morphology was observed and analyzed using SEM.

3 Results and Discussion

3.1 Flow Diameter

As demonstrated in Fig. 4a, an increase in the water-cement ratio results in a gradual enhancement of the flowability of the fresh mortar of geopolymer foam concrete. It has been established that, at a water-cement ratio of 0.5, the flowability of the fresh mortar reaches a maximum of 24.2 cm. In the event of an elevated water-cement ratio, there is a reduction in the cohesion between the foam and the mortar. This results in the foam rising to the top layer of the mortar during the mixing process. This, in turn, leads to an uneven distribution of the mortar and rupture of the foam. These factors have a detrimental effect on the performance of the concrete. Conversely, an inadequate water-to-cement ratio can result in elevated mortar viscosity, thereby compromising its flowability. This, in turn, can lead to the rupture of the foam during its formation, consequently impacting the quality of the concrete. Consequently, in the actual preparation of geopolymer foam concrete specimens, the water-to-cement ratio should be selected as 0.4 or 0.45. As demonstrated in Fig. 4b, the spread ability of the fresh mortar of geopolymer foam concrete is subject to variation in accordance with the content of RBP. It has been demonstrated that an increase in the brick powder content results in an enhancement of the spread ability of the fresh mortar. This phenomenon can be attributed to the lower reactivity of brick powder in comparison to slag. Consequently, this results in a reduced overall reaction degree of the precursor and enhanced workability. It is noteworthy that when the RBP content reaches 20%, the fresh mortar spread ability attains its maximum value of 18.9 cm. However, as the quantity of RBP continues to increase, there is a slight decrease in strength, as the brick powder surface contains numerous pores. It has been demonstrated that an elevated level of brick powder in the mortar results in an increased requirement for water, thereby reducing the mortar flowability.

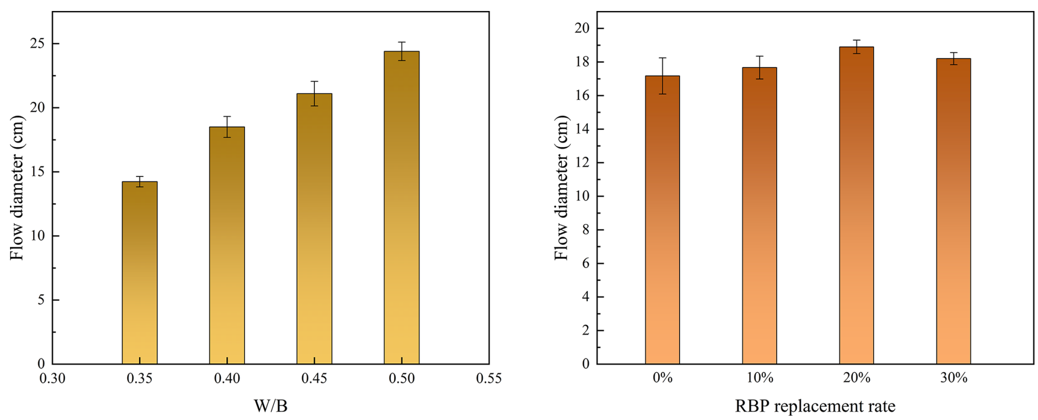

Figure 4: Flow diameter of ASRFC at (**a**) water-cement ratios, (**b**) RBP replacement rate.

3.2 Dry Density and Water Absorption

As illustrated in Fig. 5, the dry density and water absorption rate of ASRFC are shown to vary with differing water-cement ratios and brick powder content. Conversely, the dry density of ASRFC increases with the increase in RBP content. It was established that, at a water-to-binder ratio of 0.45, the dry density of the sample containing 30 wt% RBP was reduced by 5.9% in comparison with the sample devoid of RBP. Jing et al. noted that these changes may be attributed to the lower particle density and porous structure of RBP [17]. It is evident that as the brick powder content increases, the water absorption rate of ASRFC also increases. This phenomenon is primarily attributed to the lower particle density of RBP and the microstructural differences within the hardened ASRFC. RBP possesses a rough, porous surface structure, which endows it with hydrophilic properties and facilitates the absorption of free water from the slurry into the particles.

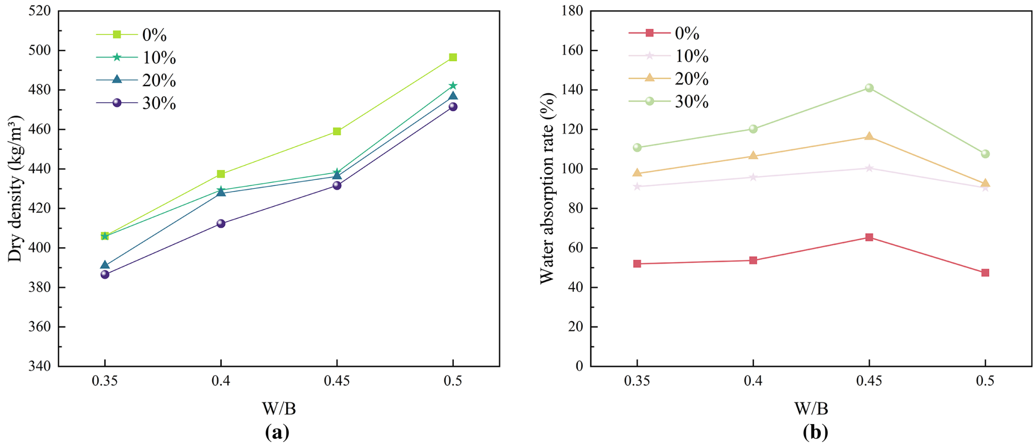

Figure 5: Effect of water-binder ratio and RBP content on (**a**) dry density and (**b**) water absorption rate of ASRFC.

Furthermore, it has been demonstrated that the water-binder ratio exerts a substantial influence on the dry density and water absorption rate of ASRFC. The dry density of ASRFC is observed to be at its maximum at a water-binder ratio of 0.5, with a range of 386 to 496 kg/m^3. When the brick powder content is 30%, reducing the water-to-binder ratio from 0.5 to 0.35 can lower the density of ASRFC from over 400 to over 300 kg/m^3. This phenomenon may be attributed to the presence of excessive and unstable bubbles in the slurry, resulting in bubble coalescence and rupture. As the water-to-binder ratio continues to increase, the water absorption rate shows an overall trend of first increasing and then decreasing, with the optimal value at 0.45. Increasing the water-to-binder ratio has been shown to increase the porosity of the foam concrete, making the pore structure more porous and thereby increasing the water absorption rate. However, an elevated water-to-binder ratio has been observed to induce bubble collapse during the foaming process, resulting in damage to the entire pore structure and a concomitant decline in water absorption rate.

3.3 Mechanical Properties

3.3.1 Compressive and Flexural Strengths

As illustrated in Fig. 6, the impact of varying water-to-binder ratios and RBP content on the compressive strength of ASRFC is examined at different curing ages. The compressive strength of all foam concrete groups (except those with 0% RBP content) reached its peak at 14 days, with a maximum value of 1.5 MPa, and showed a slight decrease at 28 days. This phenomenon can be attributed to the immersion of the alkali-activated slag in water, which results in the consumption of alkali bases and hydroxyl groups, thereby reducing the extent of the reaction. Furthermore, during the process of compressive strength testing, the presence of free water within the pores is a key factor. The water pressure exerted on the pore walls serves to augment the forces already present, thereby reducing the strength of the material. It is hypothesized that the decrease in strength may be attributed to changes in water absorption rate and density, as well as alterations in pore structure caused by water environmental conditions.

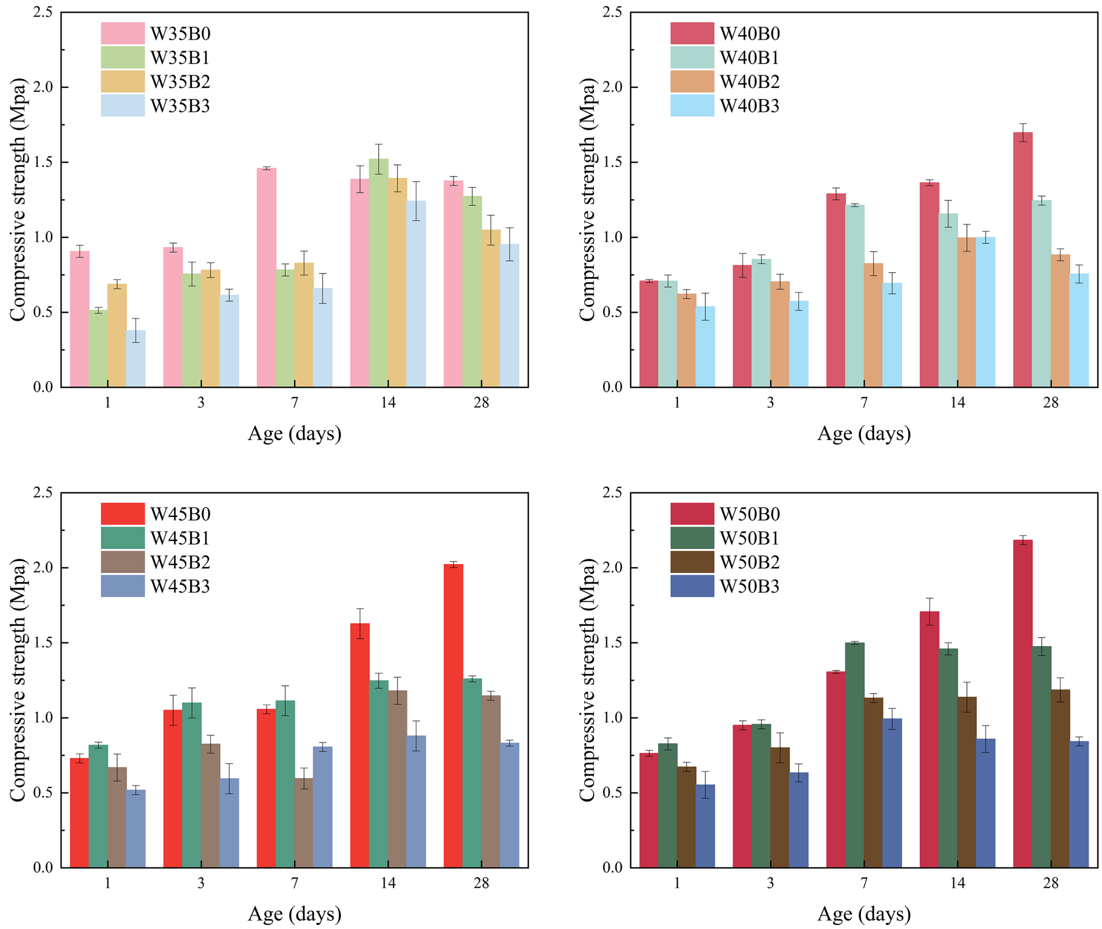

Figure 6: Age-related compressive strength of ASRFC.

The incorporation of slag, ranging from 0% to 30%, led to a decline in compressive and flexural strength after 28 days, with a decrease of 30.76%, 55.5%, 58.88%, and 61.44%, respectively, across various water-to-binder ratios of 30.76%, 55.5%, 58.88%, and 61.44%. Moreover, it has been demonstrated that the decrease in strength increases in proportion to the increase in RBP content. It is evident that, on the one hand, the presence of RBP, as an inert material, results in a delay in the geopolymerisation reaction and the formation of reaction products. Consequently, as the RBP content increases, there is a corresponding decrease in strength. Conversely, the particle size of RBP is larger than that of slag. The presence of unreacted large particles has been shown to form a weak interface transition zone with the matrix. This is prone to penetrating the pore walls under compressive stress, damaging the pore structure, and thereby reducing compressive strength. As demonstrated by the 28-day compressive strength results, the strength reduction in Group B1 was relatively insignificant. A marginal decrease was observed at a water-to-binder ratio of 0.35, indicating that the optimal RBP content is 10 wt%.

It has been demonstrated that an increase in the water-to-binder ratio enhances the compressive strength of foam concrete to a certain extent. At the 28-day stage, Group B1 at W50 exhibited compressive strength values of approximately 15.98%, 18.51%, and 17.1% higher than those at W35, W40, and W45, respectively. This enhancement is chiefly ascribed to the uniform formation of early-stage bubbles, which culminates in more uniform stress distribution within the structure, consequently leading to enhanced compressive strength.

As illustrated in Fig. 7, the flexural strength of ASRFC at varying curing ages is influenced by the ratio of water to binder, as well as the content of RBP. The compressive strength of the foam concrete in each group stabilized at 28 days, reaching a maximum of 0.8 MPa. This was primarily attributable to the continuous hydration reaction, which enhanced the overall strength of the material.

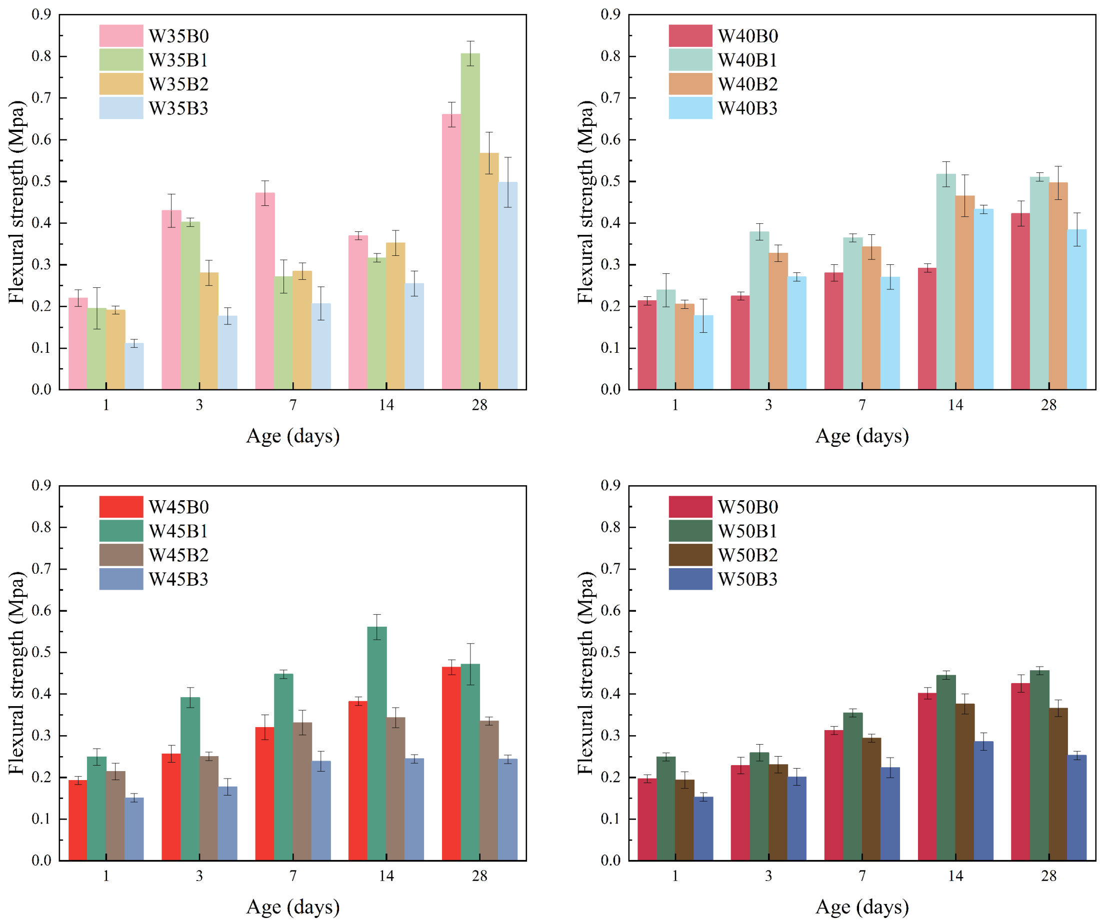

Figure 7: Age-related flexural strength of ASRFC.

It was found that when the brick powder content was 10%, the flexural strength of the foam concrete was optimal, with improvements of 22.14%, 20.62%, 1.60%, and 7.18% compared to the B0 group at 28 days for each water-to-binder ratio. Furthermore, an inverse relationship was observed between the flexural strength and the RBP content, with the strength diminishing as the content increased. The primary rationale behind this phenomenon pertains to the effective incorporation of brick powder, which has been demonstrated to efficiently fill the pores and micro-cracks within the foam concrete. This process has been shown to reduce the number of large pores and interconnected pores, thereby mitigating stress concentration. Additionally, the uniform distribution of brick powder particles in the cement paste enhances the bond strength between the matrix and pores, acting similarly to aggregate in bridging the pores. This reduces delamination between pores and the matrix, thereby improving the flexural strength of the foam concrete. However, it has been demonstrated that the addition of excessive quantities of brick powder can result in the formation of an excess of interface transition zones within the material, which has been shown to lead to a decrease in flexural strength values [12].

It has been demonstrated that an increase in the water-to-cement ratio of foam concrete results in a reduction of its flexural strength. In Group B1 at 28 days, the flexural strength values of W50 were approximately 43.47%, 10.67%, and 3.31% lower than those of W35, W40, and W45, respectively. This is primarily attributed to the reduced consistency of the mortar, increased porosity of the foam concrete, and decreased density, which collectively reduce its flexural strength.

3.3.2 Flexural-to-Compressive Strength Ratio

The ratio of flexural strength to compressive strength of foam concrete is referred to as the flexural-to-compressive strength ratio, which is one of the key indicators reflecting the ductility characteristics of foam concrete. As illustrated in Fig. 8, the flexural-to-compressive strength ratio of ASRFC is shown to be influenced by varying water-to-binder ratios and RBP content at different curing ages. The optimal dosage of RBP is demonstrated to be 10%–20%, while a water-to-binder ratio of 0.4–0.5 is recommended. The replacement of slag with RBP has been shown to enhance the flexural-to-compressive strength ratio of foam concrete, thereby improving its toughness and crack resistance under bending loads. It is noteworthy that when the slag content is 10%–20%, the flexural strength of foam concrete is optimal. This is evidenced by the significant increases observed in W40B1 and W40B2, with respective increases of 64.53% and 125.42%, in comparison to W40B0. This is primarily due to the fact that the addition of brick powder enhances the flexural strength of foam concrete, but its lower reactivity reduces compressive strength. However, the bridging effect of micro-aggregates has been demonstrated to enhance flexural strength, thereby resulting in an overall increasing trend in the flexural-to-compressive strength ratio. It has been demonstrated that an increase in the water-to-binder ratio has a detrimental effect on the ductility of foam concrete. At the 28-day stage, Group B1 exhibited a decline in the flexural-to-compressive strength ratio of W50 by approximately 51.22%, 24.62%, and 11.82%, respectively, when compared to W35, W40, and W45. This finding suggests that while augmenting the water-to-binder ratio within a specified range can yield enhanced compressive strength, the rate of deterioration in flexural strength surpasses the rate of growth in compressive strength, leading to diminished overall toughness. However, the 0.35 water-to-binder ratio demonstrates considerable variability in the flexural-to-compressive strength ratio, attributable to the uneven formation of early-stage bubbles and the subsequent loss of compressive strength in the later stages. Nonetheless, the findings of the study indicate that RBP has the capacity to enhance the toughness of foam concrete.

3.4 Thermal Conductivity

Fig. 9 presents the influence of varying water-to-binder ratios and RBP replacement rates on the thermal conductivity of ASRFC. Analytical results indicate that ASRFC demonstrates superior thermal insulation performance with lower thermal conductivity when the RBP replacement rate is 10%–20%, and the water-to-binder ratio is 0.45. The thermal conductivity of alkali-activated foam concrete exhibits distinct variations governed by the water-to-binder ratio and brick powder content. Except for Group B3, all other groups show a trend where thermal conductivity first decreases and then increases with the elevation of the water-to-binder ratio. In Group B1, the thermal conductivity values are 0.10386, 0.09617, 0.10725, and 0.11339 W/(m·K) at water-to-binder ratios of 0.35, 0.4, 0.45, and 0.5, respectively. Notably, the evolution of thermal conductivity with increasing RBP replacement rate follows a complex pattern.

At water-to-binder ratios below 0.4, thermal conductivity initially decreases and then increases with rising RBP content. Groups B1 and B2 exhibit overall lower thermal conductivity than Group B0, whereas Group W35B3 shows an 8.36% increase compared to Group W35B0. This phenomenon is primarily attributed to the formation of excessive interconnected pores due to poor porosity at low water-to-binder ratios, which weakens heat resistance and elevates thermal conductivity. Higher RBP content exacerbates this effect by acting as a heat-conductive framework, facilitating efficient heat transfer.

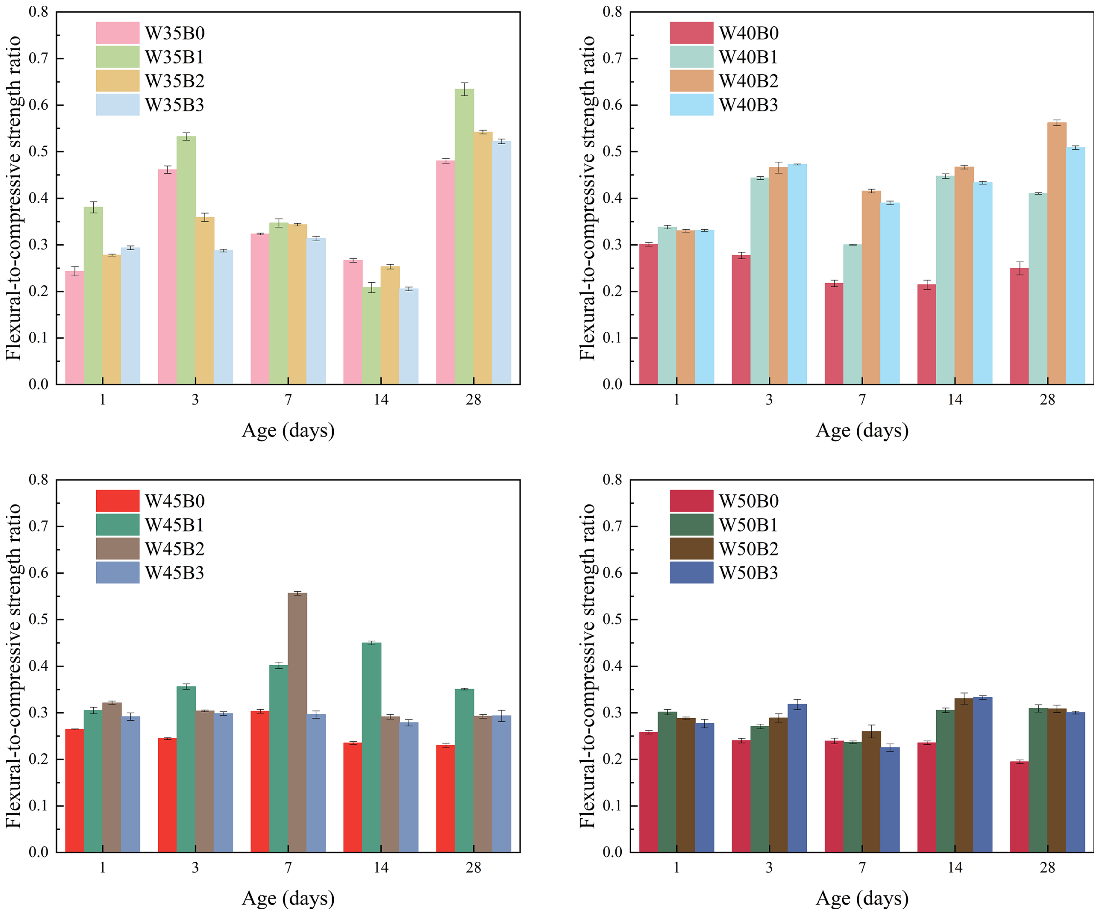

Figure 8: Age-related flexural-to-compressive strength ratio of ASRFC.

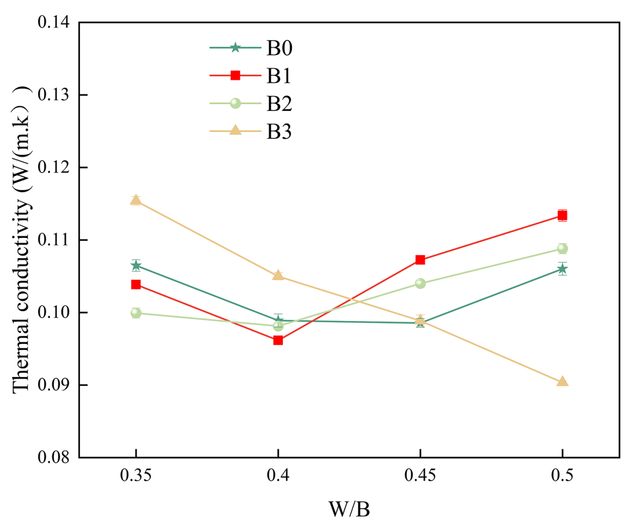

Figure 9: Thermal conductivity of ASRFC.

At water-to-binder ratios above 0.4, thermal conductivity first increases and then decreases with increasing RBP content. For instance, Group W45B1 exhibits a thermal conductivity of 0.10725 W/(m·K), representing increases of 8.82%, 3.13%, and 8.5% compared to Groups W45B0, W45B2, and W45B3, respectively. This behavior can be attributed to the retention of RBP's inherent porous structure at high water-to-binder ratios, where its low reactivity allows the preservation of microstructural features that mitigate thermal conductivity.

3.5 Pore Structure Analysis

The mechanical strength of foam concrete is predominantly governed by its pore structure, where the pore volume fraction dictates the material's density and load-bearing capacity. For the same pore volume fraction, the pore size distribution, connectivity, and morphology collectively influence the structural integrity of foam concrete.

3.5.1 Pore Fractal Dimension (FD)

In two-dimensional analyses, the FD value inherently ranges between 1 and 2. A smaller FD indicates smoother, more regular pore boundaries with minimal fractal complexity, approximating circular geometries. Conversely, a larger FD signifies more irregular pore boundaries with increased angularity, curvatures, and branching, reflecting complex microstructural configurations. Elevated pore fractal dimensions, characterized by rough and non-uniform boundaries, facilitate water infiltration and compromise the material's density and compressive strength. The FD values for each foam concrete group are tabulated in Table 3.

Table 3: Fractal dimensions of foam concrete.

Fractal Dimension	B0	B1	B2	B3	Average
W35	1.4619	1.4485	1.5150	1.4523	1.4694
W40	1.4477	1.3274	1.4856	1.5939	1.4636
W45	1.3888	1.2958	1.4994	1.4618	1.4114
W50	1.3629	1.4250	1.4297	1.5381	1.4389
Average	1.4153	1.3742	1.4824	1.5115	–

The W45B1 specimen exhibited the lowest FD (1.2958), indicative of a highly regular internal pore structure. As the water-to-binder ratio increased, the pore FD demonstrated a non-monotonic trend, first decreasing and then increasing, which correlates with the evolving roundness of pores. Higher water-to-binder ratios enhanced paste fluidity, reducing pore aggregation and mechanical damage during mixing, thereby minimizing FD. Conversely, excessive water-to-binder ratios compromised pore stability, leading to the formation of continuous interconnected pores and subsequent FD elevation.

Comparative analysis of FD across RBP contents revealed that Group B1 exhibited a significant FD reduction relative to the control group, while Groups B2 and B3 showed 4.7% and 6.8% increases, respectively. The FD reduction in Group B1 was attributed to improved paste fluidity from RBP addition, which facilitated the formation of thicker, more stable pore walls during foaming. Conversely, elevated RBP contents induced excessive pore wall thickness, destabilizing foam structures and increasing pore roughness/connectivity—detrimental to mechanical performance [18].

The pore fractal dimension directly influenced thermal conductivity trends in ASRFC. Optimal RBP dosage 10% promoted uniform pore distributions with reduced connectivity, elongating heat transfer pathways, and minimizing thermal conductivity. The W/B biphasic effect on FD mirrored its impact on thermal conductivity, with moderate water contents enhancing pore uniformity and heat resistance. These findings highlight the critical role of RBP in optimizing thermal insulation; however, RBP dosage should be constrained below 30 wt% to balance pore structure and mechanical properties.

3.5.2 Pore Size Distribution

The pore size distributions of ASRFC mixtures are illustrated in Fig. 10. The water-to-binder ratio predominantly influenced pore populations in the 0–200 μm range. At a water-to-binder ratio of 0.45, ASRFC exhibited a significantly higher proportion of 0–200 μm pores (89.54% in W45B1) compared to lower water contents, attributed to improved paste fluidity during foam stabilization. This trend aligns with FD observations, demonstrating that moderate water-to-binder ratios enhance pore roundness and uniformity, while excessive water promotes interconnected pore formation.

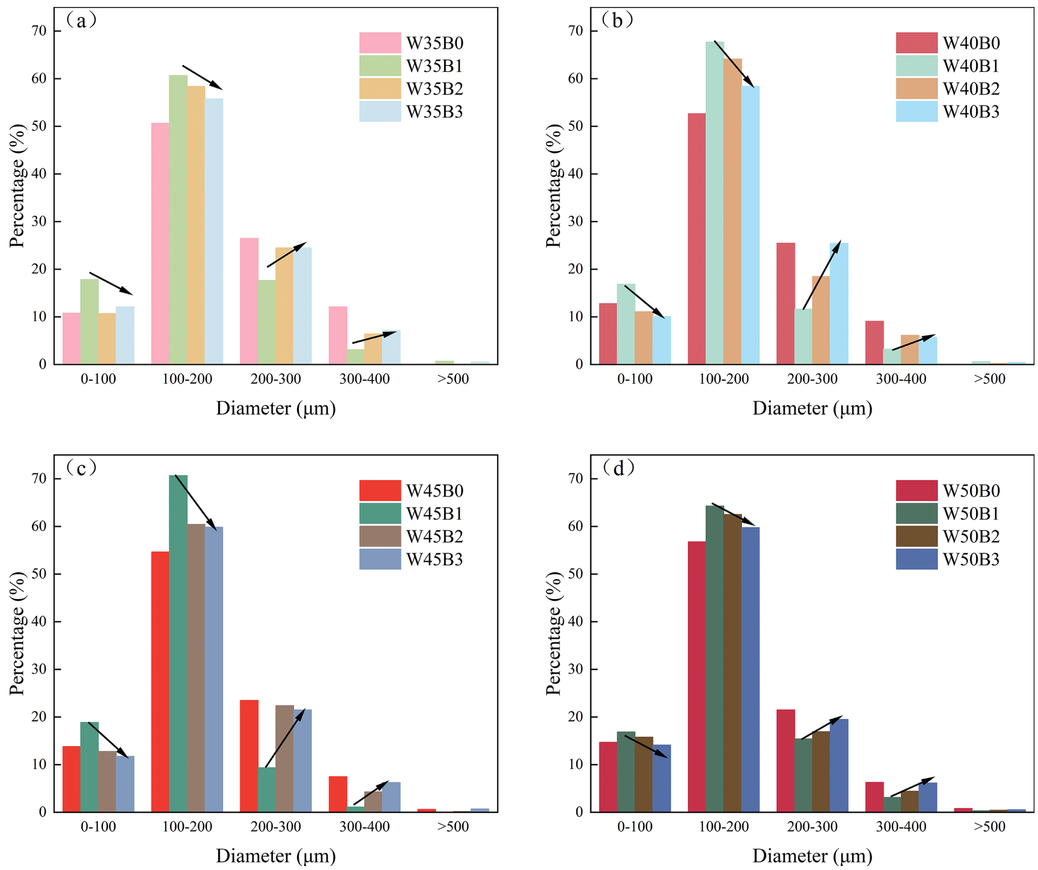

Figure 10: Influence of pore size distribution in ASRFC (**a**) W35; (**b**) W40; (**c**) W45; (**d**) W50.

RBP dosage also impacted pore size distributions: 10% RBP increased the proportion of 0–200 μm pores by ~20% relative to the control group, reducing large pore prevalence and enhancing mechanical interlock. Conversely, higher RBP contents (≥20%) shifted the distribution toward larger pores (200–300 μm), explaining the observed increases in water absorption and thermal conductivity. Mechanistically, excessive RBP introduced weak interface transition zones and destabilized foam structures, compromising load-bearing capacity and heat resistance.

The early-stage foam stability of ASRFC exerts a dominant influence on the post-curing pore characteristics and pore size distribution, thereby directly impacting heat transfer mechanisms [19,20]. Both extremely low and high water-to-binder ratios lead to suboptimal fractal dimension values and pore size distributions: the former is attributed to compromised paste fluidity, while the latter arises from insufficient structural support of pore walls during foam stabilization. The optimal incorporation of RBP in ASRFC promotes a preferential concentration of pore sizes in the small-diameter regime, reduces the formation of interconnected pore networks, and enhances the overall uniformity of pore distribution. Fig. 11 illustrates the heat transfer schematics in foam concrete with divergent pore structural configurations. Uniform, small-scale pores within the matrix significantly enhance the tortuosity of heat transfer pathways and the frequency of heat exchange, thereby augmenting internal heat storage (Q3) and optimizing the reduction in thermal conductivity.

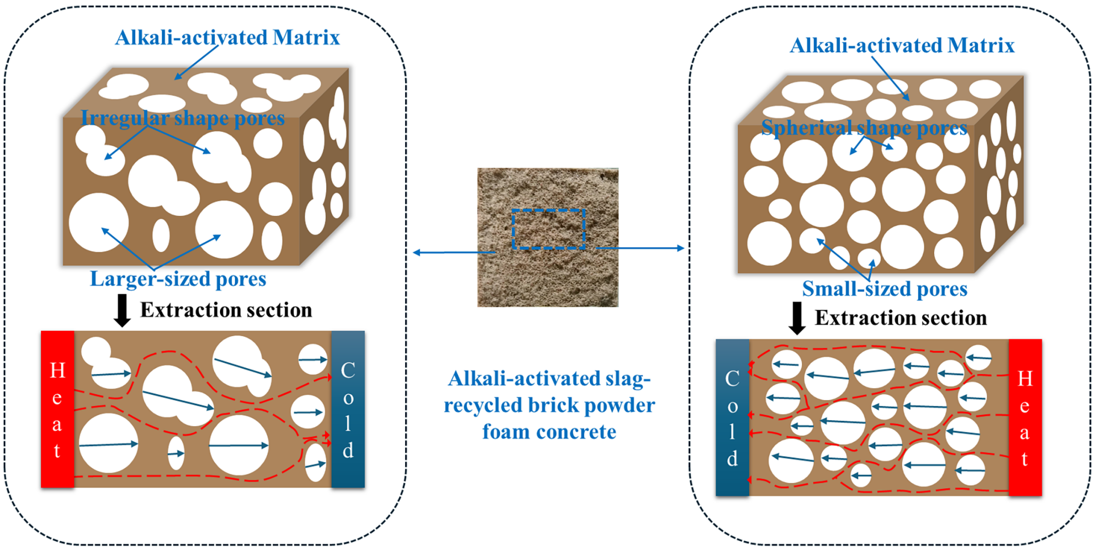

Figure 11: Schematic diagram of heat transfer in foam concrete: (**a**) Poor pore structure; (**b**) Optimized pore structure (red curve represents heat conduction path).

3.6 SEM

The SEM test results of aerated concrete at a water-to-binder ratio of 0.45 are presented in Fig. 12. It can be observed from the figure that with the continuous incorporation of BP, the pore structure of ASRFC gradually transforms from a coarse and uneven morphology to a relatively fine and uniform one, and finally evolves into a structure where pores are interconnected and partially filled.

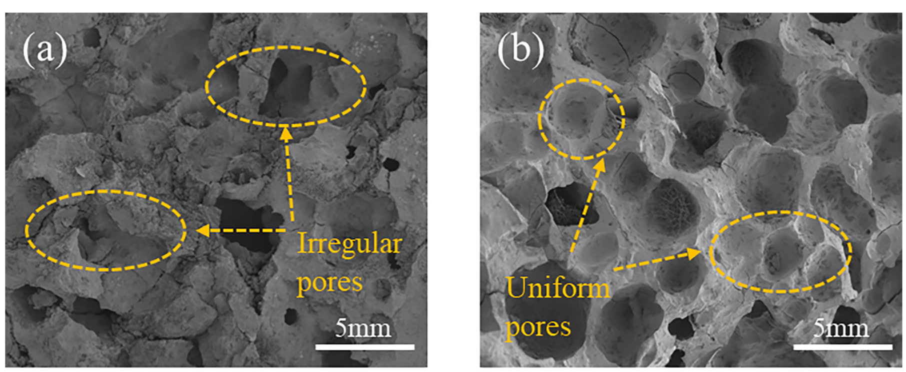

Figure 12: (Continued)

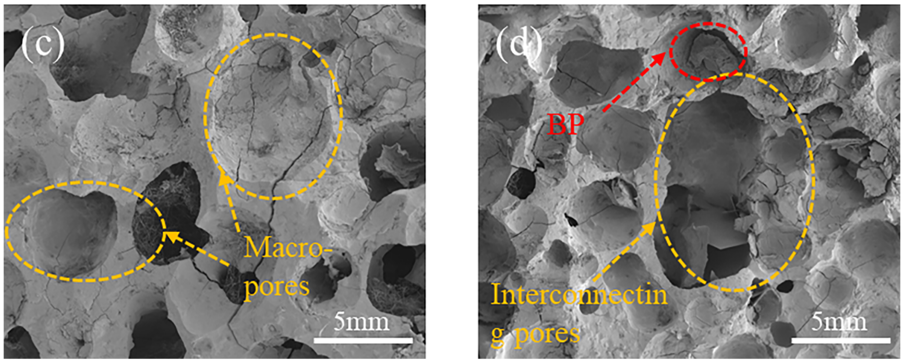

Figure 12: 50× SEM image (**a**) W45B0, (**b**) W45B1, (**c**) W45B2, (**d**) W45B3.

For the W45B0 specimen illustrated in Fig. 12a, the pore size distribution is scattered, and the thickness of the pore walls varies remarkably. Large voids and weak regions are visible locally, accompanied by complex pore shapes. The pore size distribution is highly uneven, and the pore walls appear fragile—slight collapse can be observed in certain local areas, leading to the formation of a large number of interconnected macropores. These voids inevitably serve as the primary pathways for heat conduction, essentially acting as "shortcuts" for heat transfer. In contrast, the W45B1 sample shown in Fig. 12b exhibits a significant reduction in pore size, enhanced continuity of pore walls, a more uniform pore distribution, and a more regular pore structure. The pore walls are not only thicker but also demonstrate higher stability. The addition of BP reshapes the internal skeleton of the material, forming a more robust supporting structure while mitigating the tendency of foam fusion or rupture during the foaming and curing stages. As a result, the pore network in this sample is more reliably connected; compared with the reference sample (W45B0), the stress transfer between pore walls is smoother and more controllable. Furthermore, in the W45B2 and W45B3 samples depicted in Fig. 12c,d, the number of macropores increases significantly, with the emergence of larger continuous pores. However, a phenomenon of BP redundancy within the pores also occurs: an excessive BP content can cause foam rupture during the foaming process, as BP particles cannot be encapsulated by hydration products to form an effective pore wall structure. Nevertheless, it is worth noting that the introduction of BP does provide an effective filling effect, offering sites for hydration reactions. This enables some hydration products to form within the pores, thereby reducing the connectivity of the pore structure. In summary, the appropriate incorporation of BP allows ASRFC to optimize its pore structure by regulating the pore type and pore wall density. These comprehensive improvements collectively enhance the structural strength and heat resistance of the material.

Fig. 13 presents the SEM morphologies of the samples at magnifications of ×500 and ×2000, respectively. As illustrated in Fig. 13a,e, the pore walls of the reference sample contain only scattered hydration products, with the C-S-H gel appearing as flocculent aggregates. Under this condition, the gel framework exhibits weak connectivity, leading to insufficient load-bearing capacity of the pore walls, high pore connectivity, and poor flexural strength. Fig. 13b,f shows the morphology of the W45B1 sample, which displays a distinct gel network structure within the pores. The BP particles are enveloped by hydration products, forming a relatively dense network that fills the pores, inhibits the propagation of microcracks, and thereby enhances the thermal insulation performance of the material. Fig. 13c,g depicts the microstructure of the W45B2 sample. New gel networks also form within the pores to reinforce the pore wall structure, with distinct BP particles attached; however, compared with the W45B1 sample, the network structure is relatively loose, resulting in a weaker pore-filling effect. Fig. 13d,h illustrates the microstructure of the W45B3 sample. In this case, a large number of BP particles have accumulated within the pores, and the gel structure is unable to effectively fill the internal voids, leading to a more porous internal structure.

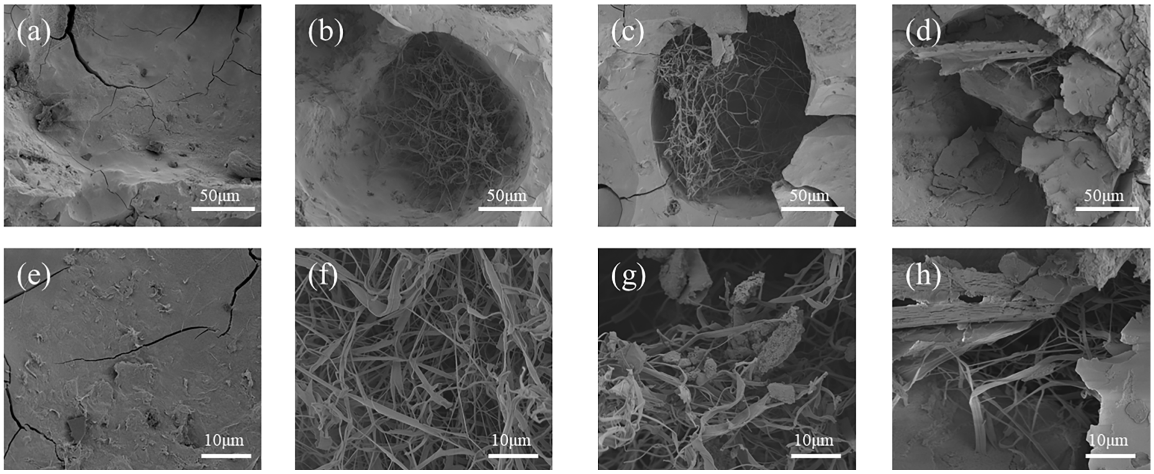

Figure 13: 500× SEM image (**a**) W45B0, (**b**) W45B1, (**c**) W45B2, (**d**) W45B3 and 2K× SEM image (**e**) W45B0, (**f**) W45B1, (**g**) W45B2, (**h**) W45B3.

3.7 XRD

Fig. 14 illustrates the XRD patterns of four ASRFC mixtures with a water-to-binder ratio of 0.45. The XRD results clearly reveal that the main crystalline and amorphous phases in ASRFC primarily consist of SiO_2, $Ca(OH)_2$, $CaCO_3$, C-(A)-S-H gel, and ettringite (AFt), with noticeable variations in peak intensity and profile among different mixtures. The incorporation of BP exerts a significant influence on the geopolymeric reaction process and modifies the assemblage of reaction products. A distinct diffraction peak corresponding to $CaCO_3$ appears at approximately 29° 2Thera, which also overlaps with the characteristic signal of C-(A)-S-H gel, a typical binding phase widely present in high-calcium alkali-activated systems. The addition of BP results in a prominent increase in SiO_2 content, whereas the contents of $Ca(OH)_2$ and $CaCO_3$ in the binder matrix gradually decrease with an increasing BP replacement ratio. The enhanced diffraction intensity of the quartz phase with rising BP dosage suggests that a considerable portion of BP participates only minimally in the pozzolanic reaction; the correspondingly reduced reaction degree consequently leads to a decline in mechanical strength. Nevertheless, fine-grained SiO_2 serves as the principal reactive component involved in the pozzolanic reaction. Thus, an appropriate dosage of BP may promote the pozzolanic reactivity of the alkali-activated binder system. On the one hand, the increased quartz phase verifies the physical filling effect of brick powder; on the other hand, the higher content of crystalline phases contributes to alleviating the volume shrinkage of the hardened matrix.

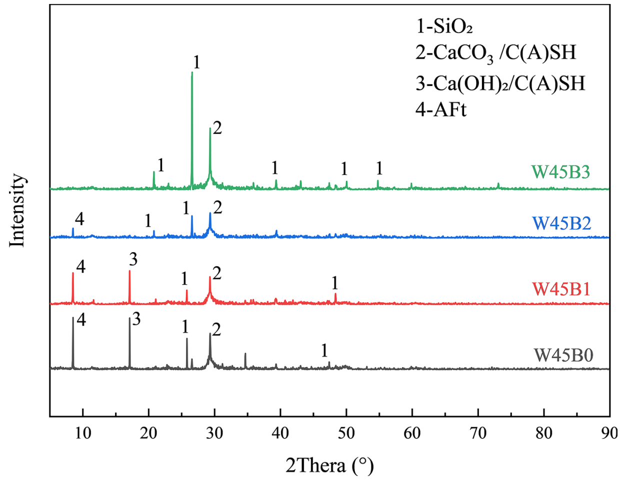

Figure 14: XRD patterns of W45B0, W45B1, W45B2, W45B3.

4 Conclusions

This study investigates the physical and mechanical properties and pore structure of ASRFC. ASRFC demonstrates the advantages of low density, moderate strength, and excellent thermal insulation, indicating its potential application in building insulation materials and as a solution for construction waste recycling. The introduction of RBP in foam concrete not only enhances its physical and mechanical properties but also optimizes thermal insulation and pore structure. The main conclusions are as follows:

1. A lightweight ASRFC with desirable strength and thermal insulation was successfully developed. At dry densities ranging from 380 to 500 kg/m^3, the material exhibited compressive strengths of 1.5–2 MPa, flexural strengths of 0.3–0.4 MPa, flexural-to-compressive strength ratios of 0.3–0.6, and thermal conductivities of 0.096–0.115 W/(m·K), meeting basic requirements for non-structural insulation components.

2. Increasing the water-to-binder ratio enhanced paste fluidity and dry density, but detrimentally affected flexural strength and toughness. Thermal conductivity displayed a non-monotonic trend, with the optimal value of 0.45 balancing workability and thermal-mechanical performance.

3. The incorporation of RBP enhances ASRFC flexural strength and improves its flexural-to-compressive strength ratio. Due to RBP porous and lightweight characteristics, ASRFC exhibits reduced dry density and increased water absorption. Notably, at a 10% RBP replacement rate, ASRFC shows superior thermal insulation due to its uniform pore structure.

4. Adding RBP leads to larger and more interconnected pores. As RBP replacement rate increases, the fractal dimension first decreases and then increases, while the pore size distribution shows a reduction in 0–200 μm pores and an increase in large pores (>200 μm). Comprehensive analysis identifies 10% RBP replacement rate as optimal. A significant correlation exists between pore fractal dimension and thermal conductivity of alkali-activated foam concrete.

Acknowledgement: The Kailuan (Group) Co., Ltd. and Science and Technology Development Fund (FDCT), Macao SAR are acknowledged.

Funding Statement: This research is supported by 2024 Science and Technology Innovation Plan Prospective Project of Kailuan (Group) Co., Ltd. (Jm2024-55) and Science and Technology Development Fund (FDCT), Macao SAR (0096/2023/AFJ).

Author Contributions: The authors confirm contribution to the paper as follows: Conceptualization, Xinzhan Li and Li Li; methodology, Xinzhan Li, Haixin Sun and Li Li; funding acquisition, Zongjin Li, Guangming Xie, Guangzhao Li and Li Li; data curation, Xinzhan Li; visualization, Xinzhan Li and Haixin Sun; writing—original draft preparation, Xinzhan Li; writing—review and editing, Xinzhan Li, Haixin Sun and Li Li; formal analysis, Xinzhan Li; validation, Xinzhan Li; investigation, Xinzhan Li; resources, Xinzhan Li; supervision, Li Li; project administration, Li Li. All authors reviewed and approved the final version of the manuscript.

Availability of Data and Materials: The datasets generated and/or analyzed during the current study are not publicly available but can be accessed upon reasonable request. Interested researchers should contact the corresponding author (Li Li) via [lili_research@163.com] to request data access, with a detailed description of the intended research use. Data sharing will be granted following the approval of the corresponding author and compliance with relevant ethical and institutional guidelines.

Ethics Approval: Not applicable.

Conflicts of Interest: Guangming Xie and Guangzhao Li are full-time employees of Kailuan Energy Chemical Co., Ltd., which also provided funding for this study. The authors affirm that they have no additional financial or personal conflicts of interest that could have influenced the work reported in this manuscript.

References

1. Tong X, Zhang Z, Zhang M, Jie Z, Gong Y. Performance evaluation of eco-friendly recycled powder in foamed concrete: influence of powder types and replacement ratios. Materials. 2025;18(23):5470. doi:10.3390/ma18235470.
2. Liu Y, Fan S, Liu Z, Che J, Liang H, Ma L, et al. Experimental study on the effects of glass hollow microspheres and fly ash on the thermo-mechanical properties, pore structure, and interface characteristics of foamed concrete. Case Stud Constr Mater. 2026;24(4):e05905. doi:10.1016/j.cscm.2026.e05905.
3. Chetharajupalli V, Prakash SS, Dirar S, Gandhi ISR. Characterization of synthetic foaming agent with additives for lightweight aggregate foam concrete applications. J Mater Civ Eng. 2026;38(7):04026201. doi:10.1061/jmcee7.mteng-21922.
4. Shah SN, Mo KH, Yap SP, Yang J, Ling TC. Lightweight foamed concrete as a promising avenue for incorporating waste materials: a review. Resour Conserv Recycl. 2021;164:105103. doi:10.1016/j.resconrec.2020.105103.
5. Abdulazeez AS, Sani AA. Properties of foam concrete: a review. Discov Concr Cem. 2026;2(1):4. doi:10.1007/s44416-026-00042-y.
6. Wagh CD, Gandhi ISR. Investigations on the performance of xanthan gum as a foam stabilizer and assessment of economic and environmental impacts of foam concrete production. J Build Eng. 2024;82:108286. doi:10.1016/j.jobe.2023.108286.
7. Fu C, Zhang H, Gong F, Jiang J. Municipal solid waste incineration bottom ash (MIBA) for high-performance, low-shrinkage, and sustainable foam concrete. Process Saf Environ Prot. 2026;211:108777. doi:10.1016/j.psep.2026.108777.
8. Bie Y, Ba S, Chen S. Studies on foamed concrete micropores and their effects on stress distribution and heat conduction. J Build Eng. 2024;87:109152. doi:10.1016/j.jobe.2024.109152.
9. Wu H, Zuo J, Zillante G, Wang J, Yuan H. Status quo and future directions of construction and demolition waste research: a critical review. J Clean Prod. 2019;240(2):118163. doi:10.1016/j.jclepro.2019.118163.
10. Wang B, Yan L, Fu Q, Kasal B. A comprehensive review on recycled aggregate and recycled aggregate concrete. Resour Conserv Recycl. 2021;171(5):105565. doi:10.1016/j.resconrec.2021.105565.
11. Du Y, Li S, Kong L, Tian J, Yuan J, Fu H. Investigation of the flow and mechanical performances of foamed concrete used for filling cracks in the base layer of asphalt pavement. Buildings. 2026;16(5):1036. doi:10.3390/buildings16051036.
12. Jin P, Li L, Li Z, Du W, Khan M, Li Z. Using recycled brick powder in slag based geopolymer foam cured at ambient temperature: strength, thermal stability and microstructure. Constr Build Mater. 2024;452:139008. doi:10.1016/j.conbuildmat.2024.139008.

13. Zhang Z, Provis JL, Reid A, Wang H. Mechanical, thermal insulation, thermal resistance and acoustic absorption properties of geopolymer foam concrete. Cem Concr Compos. 2015;62(2):97–105. doi:10.1016/j.cemconcomp.2015.03.013.
14. Wang CQ, Yu L, Liu YY, Wu K. Red mud-modified fly ash resource utilization in foamed concrete: basic performance research, hydration reaction and pore structure quantitative analysis. Chem Eng J. 2026;531(1):174180. doi:10.1016/j.cej.2026.174180.
15. Khan A, Ali A, Mehboob SS, Tayyab A, Khan D, Mursaleen M, et al. Multi-objective optimization of thermal and mechanical properties of lightweight foam concrete with Binary Blend of fly ash and silica fume. J Build Eng. 2026;120(5):115387. doi:10.1016/j.jobe.2026.115387.
16. Zhang C, Fan D, Lu JX, Pang C, Poon CS. Ultra-stable foam enabled by nano silica engineering for foam concrete improvement. Cem Concr Compos. 2024;150(2):105575. doi:10.1016/j.cemconcomp.2024.105575.
17. Jin P, Li Z, Li L, Li Z, Bao J. Development of high-water-resistance and high-strength alkali- activated foam by using waste brick powder. Constr Build Mater. 2025;467:140397. doi:10.1016/j.conbuildmat.2025.140397.
18. Dang J, Tang X, Xiao J, Duan Z, Han A. Role of recycled brick powder and alkaline solution on the properties of eco-friendly alkali-activated foam concrete. J Clean Prod. 2024;436(14):140381. doi:10.1016/j.jclepro.2023.140381.
19. Ashteyat A, Al-Ani I, Shhabat M, Aljarah AH, Al-Kroom H. Development of eco-friendly lightweight foamed concrete using waste marble powder and waste glass powder. Results Mater. 2026;29(1):100873. doi:10.1016/j.rinma.2025.100873.
20. Jiang P, Wang F, Li N, Wang W, Wang B, Yu P. Polyurethane foam lightweight concrete: preparation, CO_2 fixation properties and mechanism. J CO_2 Util. 2025;97(1):103109. doi:10.1016/j.jcou.2025.103109.